International Journal of Heat and Mass Transfer 81 (2015) 705–720

Contents lists available at ScienceDirect

International Journal of Heat and Mass Transfer

journal homepage: www.elsevier.com/locate/ijhmt

Flow boiling in microgravity: Part 1 – Interfacial behavior and experimental heat transfer results

Christopher Konishi [a], Hyoungsoon Lee [a], Issam Mudawar [a,*], Mohammad M. Hasan [b], Henry K. Nahra [b], Nancy R. Hall [b], James D. Wagner [b], Rochelle L. May [b], Jeffrey R. Mackey [c]

[a] Purdue University Boiling and Two-Phase Flow Laboratory (PU-BTPFL), School of Mechanical Engineering, 585 Purdue Mall, West Lafayette, IN 47907, USA
[b] NASA Glenn Research Center, 21000 Brookpark Road, Cleveland, OH 44135, USA
[c] Vantage Partners, LLC, 3000 Aerospace Parkway, Brook Park, OH 44142, USA

ARTICLE INFO

Article history:
Received 8 August 2014
Received in revised form 21 October 2014
Accepted 21 October 2014
Available online 21 November 2014

Keywords:
Microgravity
Flow boiling
Interfacial behavior

ABSTRACT

Space agencies worldwide are being confronted with the challenges of more distant manned space missions, which will demand greater energy efficiency and reduced weight and volume. One method being considered to reduce the weight and volume of a long duration mission spacecraft is to replace present single-phase Thermal Control Systems (TCSs) with ones that rely on flow boiling and condensation. This transition will require a thorough understanding of the influence of reduced gravity on flow boiling and condensation, and the development of predictive tools for both. This study is the first part of a two-part study investigating flow boiling of FC-72 in microgravity, which is simulated in a series of parabolic flight maneuvers. Flow boiling experiments are conducted in a rectangular channel fitted with two opposite heating walls. The operating conditions include liquid inlet velocities of 0.1–1.9 m/s, liquid mass velocities of 224.2–3347.5 kg/m^2 s, and inlet subcoolings ranging from 2.8 to 8.1 °C. The study includes both high-speed video analysis of interfacial features and heat transfer measurements. A dominant wavy vapor layer behavior is encountered for most operating conditions. Boiling is sustained mostly in 'wetting fronts' corresponding to contact regions between the wave troughs and the wall, and abated near the wave peaks. During a flight parabola, the heated wall temperatures decrease slightly as the aircraft enters the hypergravity ascent phase, then increase slightly during the microgravity phase, and decrease once again during the hypergravity descent. These temperature variations point to enhancement in flow boiling heat transfer with increasing gravity, and conversely a reduction with microgravity.

© 2014 Published by Elsevier Ltd.

1. Introduction

1.1. Importance of flow boiling and condensation to future space missions

Future manned space missions are expected to greatly increase in distance, duration and therefore power requirements. Feasibility of proposed missions is highly dependent on the ability to enhance energy efficiency and reduce both weight and volume. A key component where reductions in weight and volume are being sought is the Thermal Control System (TCS), which is responsible for maintaining temperature and humidity inside the space vehicle or planetary habitat. These reductions are possible with orders of magnitude enhancement in heat transfer coefficients in a TCS utilizing flow boiling and condensation, compared to TCS utilizing single-phase liquid [1,2]. A key drawback of single-phase TCS is reliance on sensible heat alone to both acquire and reject the heat. Two-phase TCS, on the other hand, capitalize on both latent and sensible heat to acquire the heat from cabin and avionics, and reject it via a condenser/radiator to deep space. However, implementation of flow boiling and condensation in future space missions will require a thorough understanding of how these heat transfer modes are influenced by reduced gravity. The present study concerns the influence of reduced gravity on flow boiling.

1.2. Pool boiling in microgravity

Research on boiling heat transfer in reduced gravity has been conducted since the late 1950s. However, most of this research has been focused on pool boiling in microgravity (μg_e). In terrestrial conditions, pool boiling relies on buoyancy to both remove bubbles from the heated wall and sustain liquid replenishment of

* Corresponding author. Tel.: +1 (765) 494 5705; fax: +1 (765) 494 0539.
E-mail address: mudawar@ecn.purdue.edu (I. Mudawar).
URL: https://engineering.purdue.edu/BTPFL (I. Mudawar).

http://dx.doi.org/10.1016/j.ijheatmasstransfer.2014.10.049
0017-9310/© 2014 Published by Elsevier Ltd.

Nomenclature

c_p	specific heat at constant pressure
G	mass velocity
g	gravity
g_e	Earth's gravitational acceleration
g_z	vertical acceleration
H	height of flow channel's cross-section
H_1	heated wall 1
H_2	heated wall 2
h	heat transfer coefficient
h_{fg}	latent heat of vaporization
k	thermal conductivity
L_d	development length of channel
L_e	exit length of channel
L_h	heated length of channel
$\dot{m}$	mass flow rate
p	pressure
q''_w	wall heat flux
q''_m	critical heat flux (CHF)
T	temperature
t	time
T_{in}	inlet temperature
T_{sat}	saturation temperature
T_w	wall temperature
$\Delta T_{sub,in}$	inlet subcooling, $T_{sat} - T_{in}$
U	mean inlet liquid velocity
W	width of flow channel's cross-section
x_e	thermodynamic equilibrium quality
z	axial distance

Greek symbols

δ_h	thickness of heated wall
λ	vapor wavelength
ρ	density

Subscripts

avg	average
asymp	asymptotic
d	developing
e	exit
f	saturated liquid; bulk liquid
g	saturated vapor
h	heated wall
in	inlet to heated portion of flow channel
m	maximum (CHF); heated wall identifier ($m = 1$ for H_1, $m = 2$ for H_2)
n	thermocouple location along heated wall
o	outlet from heated portion of flow channel
sat	saturation
sub	subcooling
w	wall

the wall. Proportional to the product of density difference between liquid and vapor, and gravity, buoyancy is greatly diminished in reduced gravity, and virtually nonexistent in μg_e. Without buoyancy, bubble nucleation, growth and coalescence in μg_e pool boiling are influenced by other effects, such as thermocapillary or Marangoni convection, which are typically masked by buoyancy in terrestrial ($1 - g_e$) conditions. Oka and coworkers performed μg_e pool boiling experiments with n-Pentane, R-113 and water [3]. At high heat fluxes and/or near-saturated conditions, isolated bubbles grew larger and coalesced with other bubbles with greater frequency, culminating in the formation of a single large bubble that encompassed the majority of the heater surface. Overall, nucleate boiling was far less effective and critical heat flux (CHF) significantly smaller in microgravity than at $1 - g_e$. Formation of a very large bubble that is responsible for low CHF in μg_e pool boiling has also been confirmed by several other investigators, including Straub et al. [4], Merte [5], Kim et al. [6] and Dhir et al. [7].

1.3. Flow patterns in microgravity adiabatic two-phase flow

Despite the important fundamental knowledge gained from μg_e pool boiling experiments, overriding concerns related to both the unusually large bubble that engulfs the heated wall, and appreciable reduction in CHF, point to serious challenges in implementing pool boiling in space applications. These concerns point to the need for another force to overcome these effects. By relying on fluid inertia to dwarf other forces, flow boiling systems provide an effective means to controlling bubble growth and maintaining liquid replenishment of the heater surface to boost CHF.

Although μg_e phase change literature spans over half a century, the vast majority of this literature concerns pool boiling and adiabatic two-phase flow patterns. On the other hand, studies concerning μg_e flow boiling are comparatively quite sparse. Since the early adiabatic two-phase microgravity experiments of Hepner et al. [8], researchers quickly realized the vast differences in interfacial behavior between μg_e and $1 - g_e$ environments. Only three of the classical flow patterns in tubes are prominently achieved in μg_e: bubbly, slug and annular flows. Investigators studied the various influences of tube diameter and fluid properties, especially surface tension, to derive relations for transitions between flow patterns. The flow pattern studies by Dukler et al. [9] and Colin et al. [10] have been verified or modified by others in pursuit of better predictions.

1.4. Flow patterns in microgravity flow boiling

Far fewer studies have examined two-phase flow patterns in flow boiling. Misawa [11] performed both drop tower and parabolic flight experiments to investigate flow boiling of R-113 in μg_e. They used a square channel (5×5 mm^2 by 500-mm long) equipped with heating film, and two electrically heated coiled tubes (4.0 and 12.8-mm diameter, 500 and 480-mm long). Flow patterns transitioned earlier in μg_e compared to $1 - g_e$, but differences in flow behavior diminished at high vapor quality. Transitions between flow patterns agreed well with the μg_e maps of Dukler et al. [9] and Colin et al. [10]. Saito et al. [12] performed parabolic flight water flow boiling experiments in a square channel (25×25 mm^2 by 600-mm long) that was fitted with an electrically heated rod (8-mm diameter by 200-mm long) along its central axis. Body force effects were prevalent at $1 - g_e$ and low flow rates, where bubbles generated on the heated rod detached and stratified in the upper portion of the flow channel. On the other hand, absence of buoyancy in μg_e caused bubble detachment to abate; bubbles continued to propagate along the heated wall. Ohta et al. [13] conducted μg_e and $2 - g_e$ parabolic flight experiments in addition to $1 - g_e$ terrestrial flow boiling experiments using R-113 flowing through 8-mm diameter Pyrex tubes (heated lengths of 70 and 255 mm) that were coated internally with thin heating gold film. At a relatively low mass velocity of $G = 150$ kg/m^2 s, bubbles in μg_e were significantly larger than in $1 - g_e$ and $2 - g_e$, whereas at $G = 600$ kg/m^{2}s, they had similar detachment diameters for all gravity levels. This similarity was attributed to increased fluid inertia dwarfing body force effects by providing sufficient interfacial shear to detach bubbles

from the heater surface before they could grow further due to evaporation. Another μg_e flow boiling flow pattern study by Celeta et al. [14] confirmed the transition criteria of Dukler et al. [9] for small diameter tubes.

1.5. Heat transfer in microgravity flow boiling

Misawa [11], Ohta et al. [13], Celeta et al. [15], Baltis et al. [16] and Luciani et al. [17,18] specifically addressed the influence of reduced gravity on two-phase heat transfer. Misawa [11] investigated the contributions of turbulence in bubbly flow. Because of the absence of drift in μg_e, they postulated that turbulence induced by bubble agitation is compromised, which weakens heat transfer in μg_e compared to $1 - g_e$. Ohta et al. [13] performed flow boiling experiments in parabolic flight at μg_e and $2 - g_e$, which they compared with ground $1 - g_e$ vertical upflow tests. For mass velocities yielding bubbly flow, changes in gravity during parabolic flight had minimal effects on heat transfer, suggesting a dominant nucleate boiling heat transfer mechanism for bubbly flow confined to the heated wall. For conditions yielding annular flow with moderate inlet quality, heat transfer at low heat fluxes was governed by two-phase forced convection and strongly influenced by gravity; here, heat transfer deteriorated in μg_e. For annular flow and high heat flux, nucleate boiling was observed within the annular liquid film, yielding similar heat transfer coefficients through the varying gravity event. Yet, the influence of gravity on annular heat transfer diminished at high inlet quality, where stronger shear forces resulting from increased vapor core velocity overcame body force effects. Celeta et al. [15] and Baltis et al. [16] explored wall temperature variations in a 6.0-mm tube with varying gravity during parabolic maneuvers. At low mass velocity and low exit vapor quality, the hypergravity phase produced bubbly flow with small bubbles detaching from the wall. Entering the μg_e phase, heat transfer was enhanced significantly in the inlet, a phenomenon they attributed to greater mixing and turbulence brought about by larger bubble diameters in μg_e. With increased mass velocity, no significant variations in wall temperature were detected, proving these operating conditions greatly reduced the influence of body force. Unlike most investigators, Luciani et al. [17,18] reported heat transfer enhancement in all μg_e conditions, with average heat transfer coefficients as much as 30% higher than $1 - g_e$ terrestrial data.

1.6. Objectives of study

Overall, the influence of body force on two-phase heat transfer appears to be highly dependent on mass velocity, inlet quality and heat flux, which also dictate flow pattern. Also, findings by different investigators often appear contradictory to one another. Clearly, there is a severe shortage of data for two-phase heat transfer in μg_e. The present two-part study fills this gap by providing detailed heat transfer data for FC-72 in a rectangular channel. The data are also complemented by extensive high-speed images that capture interfacial behavior for different flow velocities and wall heat fluxes. The first part of the study will explore the experimental methods used, heat transfer data trends, and interfacial behavior. The second part [19] will be dedicated exclusively to CHF data and development of a mechanistic CHF model.

This study is part of a NASA project with the goal of developing the Flow Boiling and Condensation Experiment (FBCE) for the International Space Station (ISS). The long-term objectives of this effort are to: (a) obtain flow boiling and condensation databases in microgravity, (b) develop an experimentally validated, mechanistic model for flow boiling critical heat flux (CHF) in microgravity, and criteria to predict the minimum flow rate required to ensure gravity-independent CHF, and (c) develop an experimentally validated, mechanistic model for condensation in microgravity, and criteria to predict the minimum flow rate required to ensure gravity-independent annular condensation. This study concerns the flow boiling portion of the project.

2. Experimental methods

2.1. Flow boiling facility

Microgravity is achieved in this study by flying a complete flow boiling facility in a series of parabolic maneuvers onboard Zero-G Corporation's modified Boeing 727 aircraft. Fig. 1(a) shows a schematic of the two-phase flow loop that is used to deliver the working fluid, FC-72, to the Flow Boiling Module (FBM) at desired pressure, temperature, and flow rate. FC-72 is a dielectric liquid with a relatively moderate saturation temperature 56 °C at atmospheric pressure. The system is deaerated to rid the FC-72 from any non-condensable gases prior to a series of tests. The deaeration is achieved in situ utilizing the Watlow Cast X-500 preheater heater to boil the circulating FC-72. A partially full fluid container is plumbed into the system at the fill and drain ports where the non-condensables are vented out. The vessel is then fully disconnected from the flow loop prior to loading the facility onto the aircraft.

The deaerated FC-72 is circulated through the closed flow loop with the aid of a magnetically coupled pump. FC-72 liquid exiting the pump is passed through a control valve, particulate filter, and a turbine flow meter. It then enters a Watlow CAST X-500 circulation heater, where the liquid temperature is raised to the desired level, before entering the FBM. The liquid is heated along the FBM, and converted to a two-phase mixture. The mixture exiting the FBM is returned to liquid state after passing through a liquid-to-air heat exchanger. Located downstream of the heat exchanger is a nitrogen-filled accumulator which is used to set a reference pressure point for the loop.

The entire flow boiling parabolic flight facility, including the flow loop components, data acquisition system, power and instrumentation cabinets, and high-speed camera, are mounted onto a rigid extruded aluminum frame as shown in Fig. 1(b).

2.2. Flow Boiling Module (FBM)

The FBM is designed to simultaneously enable thermal measurements and conduct high-speed video motion analysis of interfacial features. As shown in the exploded view in Fig. 2(a), the FBM consists of three transparent polycarbonate plastic (Lexan) plates that are bolted together between two aluminum support plates. The purpose of the support plates is to prevent buckling of the plastic plates and help prevent fluid leaks during the aircraft experiments. A rectangular flow channel is formed by cutting a 5.0-mm high by 2.5-mm wide slot into the central axis of the channel sidewall plate. The inner surfaces that form the front and back wall of the flow boiling channel are cross-polished to optical quality in order to backlight and image the flow. Both the outer channel top and bottom plastic plates are milled out to insert 15.5-mm wide, 114.6-mm long and 1.04-mm thick oxygen-free copper slabs that serve as heating walls for the FBM. O-rings are inserted in grooves milled around the perimeter of the copper plates in both the outer top and bottom plastic plates. There are two additional o-rings between the channel sidewall plate and outer top and bottom plastic plates. These o-rings ensure a leak-proof assembly.

Fig. 2(b) depicts an assembled view of the FBM. Static pressure is measured at various locations along the central axis of the flow channel using four pressure taps in the top plastic plate placed equidistantly between the FC-72 inlet port and immediately

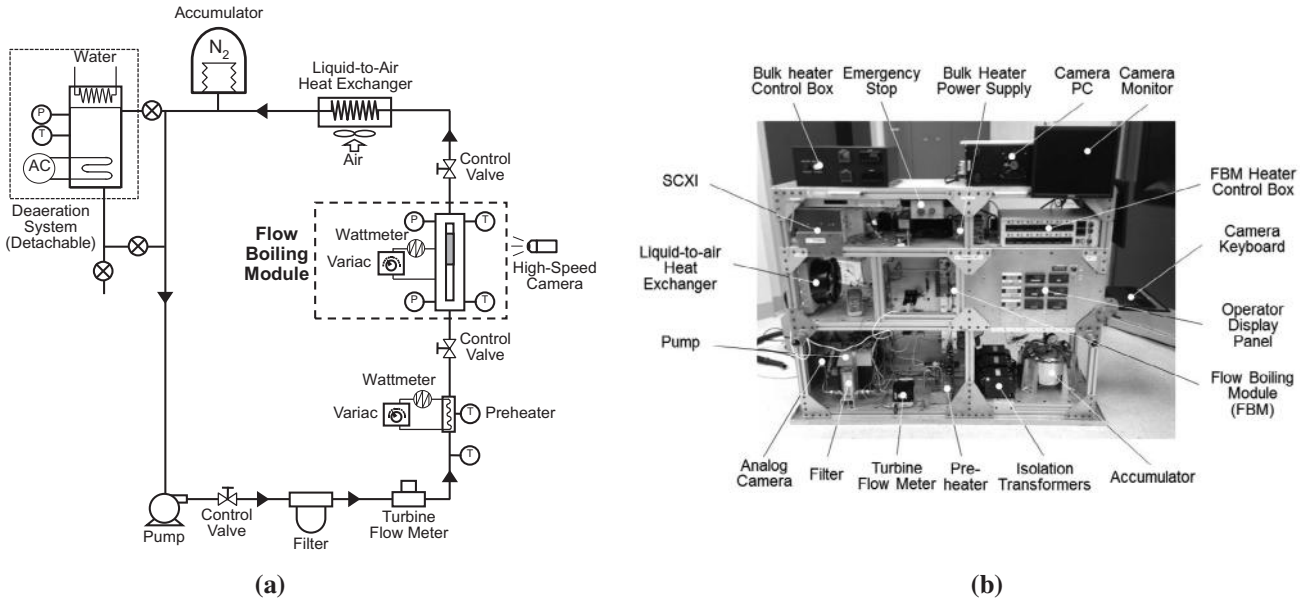

Fig. 1. (a) Schematic diagram of flow loop. (b) Photo of parabolic flight facility.

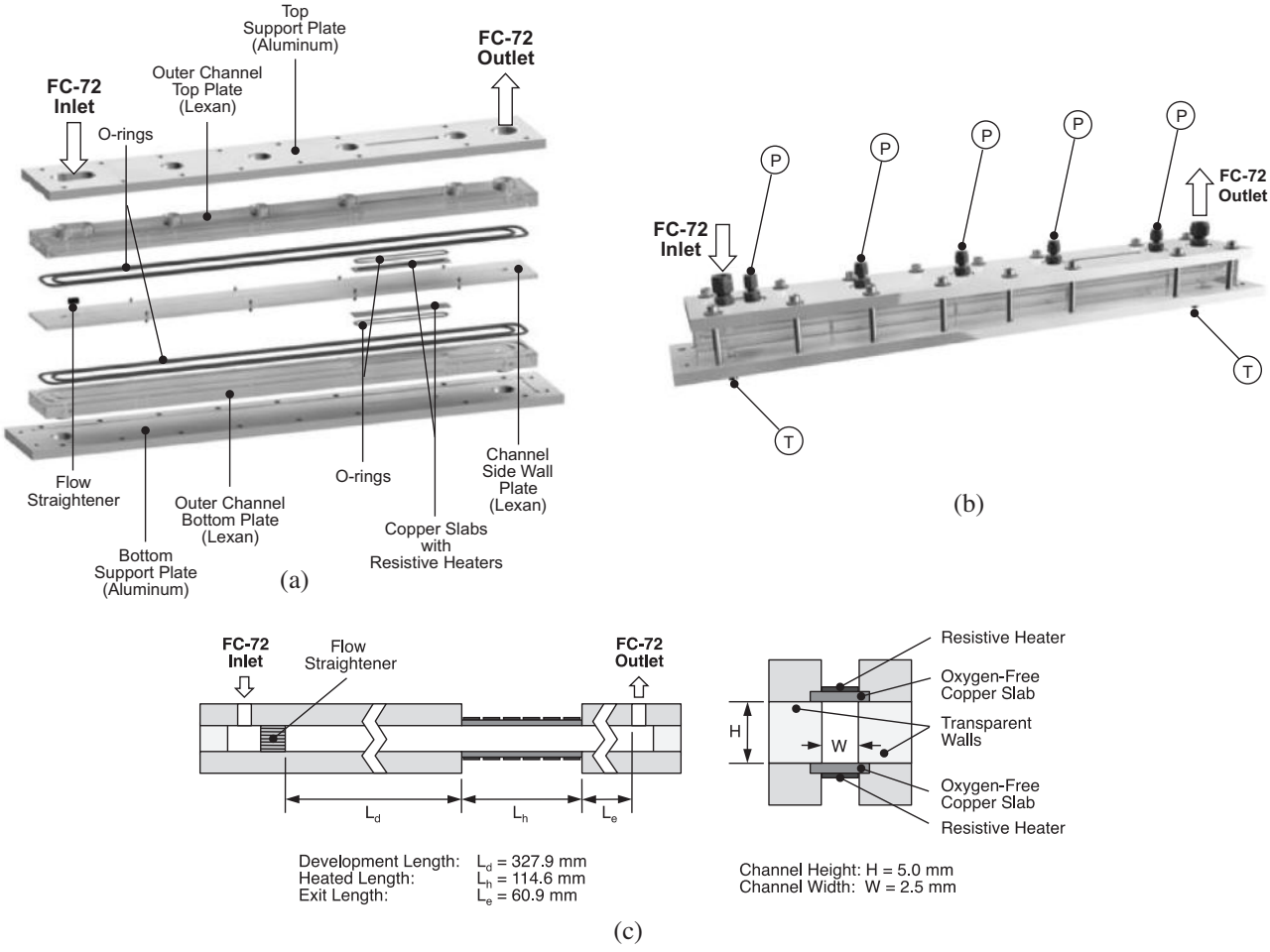

Fig. 2. (a) Exploded view of Flow Boiling Module (FBM). (b) Assembled view of FBM. (c) Key dimensions of flow channel.

upstream of the copper heating slabs, with an additional pressure tap placed downstream of the copper slabs. Type-E thermocouples are inserted in the middle of the flow channel through the bottom plastic plate near the inlet and outlet FC-72 ports.

Shown in Fig. 2(c) is a honeycomb flow straightener affixed upstream at the channel inlet to break any eddies and help straighten the flow. An entry development length 100 times the channel hydraulic diameter provides a hydrodynamically fully

developed flow prior to reaching the copper heating slabs. Indicated in Fig. 2(c) are key dimensions of the channel, including flow development length, L_d = 327.9 mm, heated length, L_h = 114.6 mm, and exit length, L_e = 60.9 mm, in addition to the height, H = 5.0 mm, and width, W = 2.5 mm of the channel's cross-section. Notice that the flow is heated along the shorter dimension, W, of the flow channel. The heated portion of the channel consists of the two thin copper slabs, placed opposite to one another, with the central transparent polycarbonate plate providing sidewalls for the rectangular flow area. The FBM is fixed securely to the facility's aluminum frame in a vertical position perpendicular to the floor of the aircraft.

2.3. Heated wall construction

As shown in Fig. 3(a), each heated wall consists of six 4.5-mm wide and 16.4-mm long thick-film resistors. Soldered in series to the backside of the copper slab, each resistor has a resistance of about 188 Ω, and each set of seven resistors per copper slab is connected electrically in parallel. Power to the resistors is supplied from a variable voltage transformer. The FBM heater control box depicted in Fig. 1(b) allows the user to supply heat to either or both heated walls at a time. As shown in Fig. 3(b), two sets of seven Type-E thermocouples are inserted into shallow indentations along the centerline of each copper plate between the resistors. One set is used for temperature measurements, and the other to activate a relay that cuts off power supply once CHF is detected. The thermocouples temperatures are designated as $T_{wm,n}$, where m represents the heated wall (H_1 or H_2) and n the axial thermocouple location.

A key concern in the present experiments is to measure the CHF that is independent of the heated wall thickness and representative of practical engineering surfaces. As discussed by Zhang et al. [20], this measurement required a minimum heated wall thickness that is dependent on the heat diffusion properties of the wall material. As shown in Fig. 3(c), CHF for FC-72 on a copper wall is dependent on wall thickness for thicknesses below 0.4 mm. Above 0.4 mm is

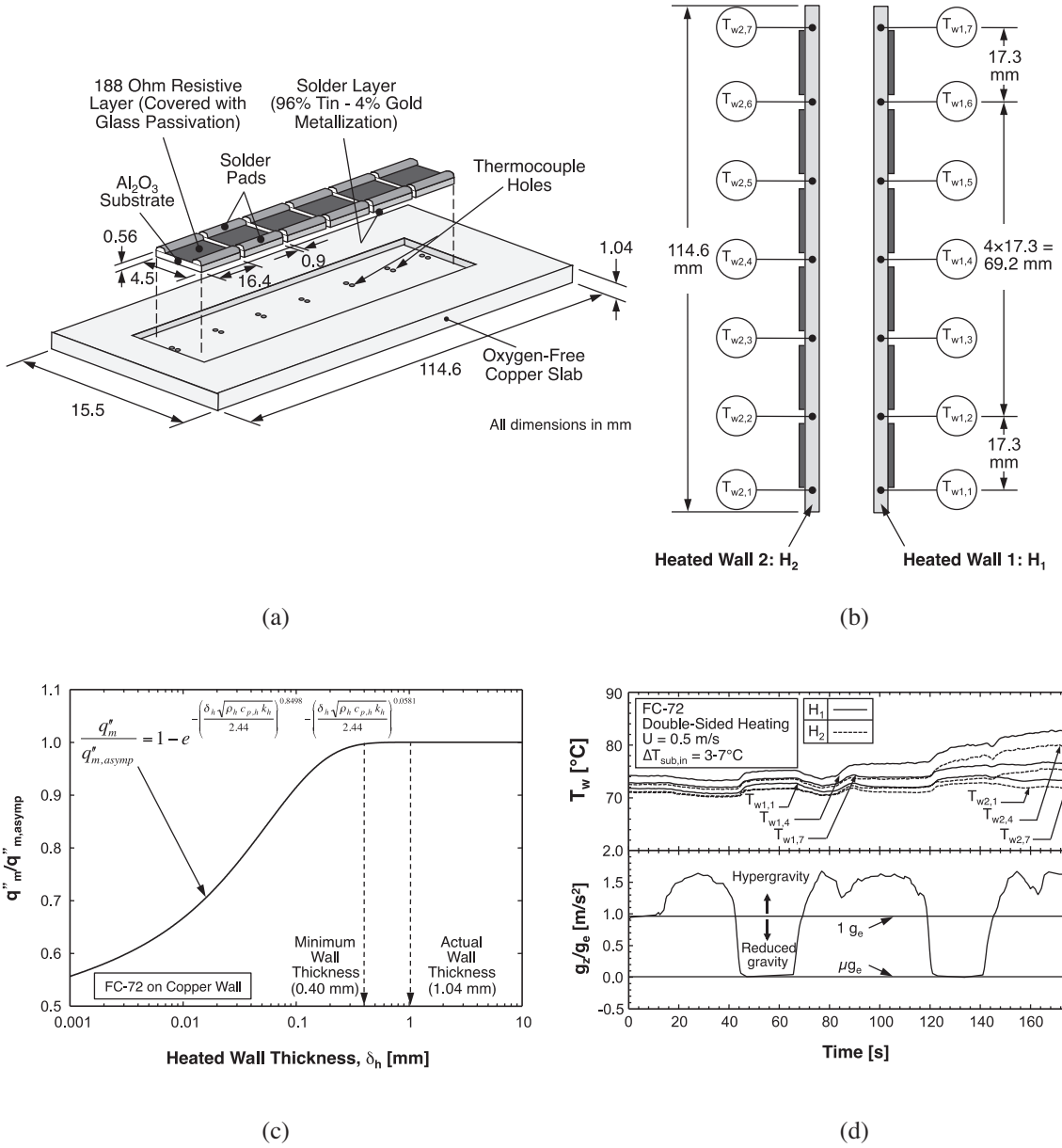

Fig. 3. (a) Construction of heated wall and thick-film resistors. (b) Thermocouple layout in two heated walls. (c) Minimum heated wall thickness requirement [20]. (d) Temporal records of heated walls' thermocouples and gravity during series of parabolas.

the asymptotic range, where CHF is both constant and independent of wall thickness. This is the desired range representative of practical surfaces. While any thickness larger than 0.4 mm is adequate, use of a very large thickness is also undesirable because this would preclude the ability of the heated wall temperatures to reach steady state during the μg_e phase of a parabola of 15–22 s. Therefore, a wall thickness of 1.04 mm is used. Fig. 3(d) shows actual temporal records of wall temperatures measured in the inlet, middle, and downstream regions of the heated copper walls and corresponding gravity record for a mean FC-72 inlet velocity of U = 0.5 m/s and $\Delta T_{sub,in}$ = 3–7 °C. These results indicate steady state conditions are achieved during the μg_e phase of the parabola.

2.4. Flow visualization techniques

A high-speed camera is used to capture the two-phase interfacial features along the heated portion of the flow channel. A fixed frame rate of 2217 frames per second (fps) and a pixel resolution of 2040 × 156 are used to capture the entire heated length for each test run. Each video image sequence consists of 3000 frames, or 1.353 s of flow visualization data per test run. Illumination is provided from the backside of the flow channel by two LEDs, with a light shaping diffuser (LSD) situated between the LEDs and the channel to enhance illumination uniformity.

It should be noted that the captured high-speed images suffer from two physical issues that cause distortion and defocus. The first is barrel distortion caused by the camera lens. As shown in Fig. 4(a), the images are obtained starting at pixel element (0,0) and ending at pixel element (2040, 156) to produce images 2040 pixels horizontally by 156 pixels vertically. The apparent curvature seen in the images is an artifact of forming the image on the pixel elements near the edge of the field of view. The second noticeable issue is the defocus or 'fuzzy' sections near the top and bottom of a boiling image. As depicted in Fig. 4(b), the copper heaters are recessed into the top and bottom polycarbonate plates so the bubbles seen near these extremes are being viewed through additional polycarbonate material that has been machined but not optically polished.

2.5. Operating conditions and measurement accuracy

As indicated earlier, the flow boiling experiments were conducted in simulated reduced gravity conditions onboard Zero-G Corporation's modified Boeing 727 parabolic flight aircraft. Four flights were performed, with a series of 40 parabolic maneuvers executed during each flight. As shown in Fig. 3(d), a single parabolic maneuver is initiated as the aircraft ascends in altitude, entering a hypergravity phase (1.5 – g_e to 1.8 – g_e). The μg_e phase is initiated just prior to the aircraft reaching the zenith of the parabolic trajectory, lasting approximately 15–22 s before entering another hypergravity phase.

The operating conditions for the study are as follows: FC-72 inlet mean liquid velocity of U = 0.1–1.9 m/s, liquid mass velocity of G = 224.2–3347.5 kg/m^2 s, inlet temperature of T_{in} = 56.5–64.7 °C, inlet subcooling of $\Delta T_{sub,in}$ = 2.8–8.1 °C, and outlet pressure of p_o = 118.2 – 148.3 kPa (17.1–21.5 psi). The desired flow conditions are set by adjusting various components of the flow loop prior to a parabolic maneuver. Once inlet conditions to the FBM are achieved, power is supplied to the FBM's copper wall resistors in the first few seconds of the microgravity period of each parabola and held constant thereafter until the beginning of the following parabola. The high-speed camera is manually triggered to record approximately 10 s into the μg_e phase. Immediately after the μg_e duration, heat flux to the FBM heaters is increased 1–5 W/cm^2, and this process is continued for each subsequent parabola until CHF is detected. A Labview program is developed in conjunction with a NI SCXI-1000 data acquisition system to record all instrument data throughout the flow boiling facility, and a special fail-safe feature is implemented into the program to automatically cut off power input to the FBM resistive heaters should any of the measured temperatures exceed 130 °C. This safety feature is

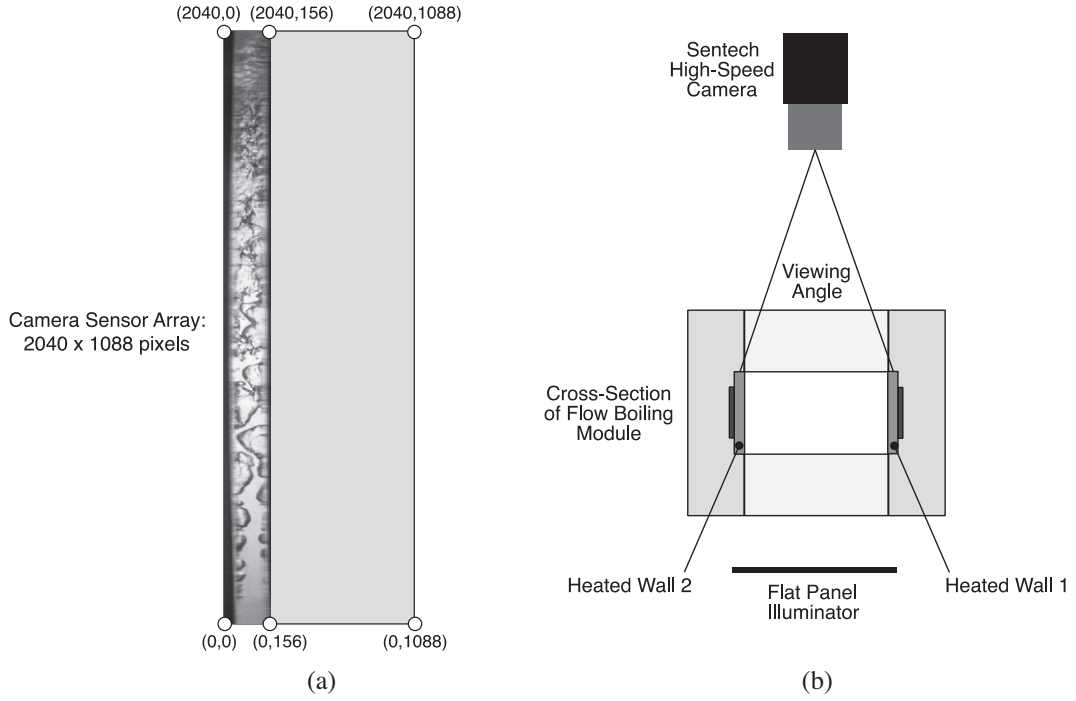

Fig. 4. (a) Resolution of high-speed video camera image encompassing entire heated region of flow channel. (b) Viewing angle of camera and back lighting.

intended to prevent any breakdown of the FC-72, which may lead to formation of the toxic compound perfluoroisobutene (PFiB).

Flow boiling tests were performed on three days of parabolic flight where both copper heated walls were activated in the FBM, and on one day where only one heated wall was activated. It should be noted that during two of the three days with both wall heated activated, unexpected technical problems with the flow boiling facility arose resulting in sporadic loss of wall temperature signals. Any of the data from tests where these anomalies occurred are excluded from data processing or presentation.

Fluid and wall temperatures throughout the flow boiling loop are measured with Type-E thermocouples having an accuracy of ±0.5 °C. STS absolute pressure transducers having an accuracy of ±0.05% are used to measure pressures at several locations along the FBM and the flow loop. The turbine flow meter has an accuracy of ±0.1%, and the accuracy of the FBM heaters is ±0.5 W while it is ±1 W for the preheater.

3.1. Flow visualization results

3.1. Interfacial features for single-sided heating

As indicated earlier, the operator of the present facility could activate either one of the heated walls (H_1) or both wall (H_1 and H_2) simultaneously. Capturing single-wall interfacial images sequences and data allows results from the present study to be compared to several prior studies that have been conducted at the PU-BTPFL that utilized one-sided heating wall. They include terrestrial studies on pool boiling on a short vertical wall [21], flow boiling on a short vertical wall [22,23], flow boiling on a long horizontal wall [24,25], and flow boiling on a long wall at different orientations relative to Earth gravity [26–32]. They also include flow boiling studies that were performed in parabolic flight to simulate microgravity [20,33–35]. A fundamental reason for using a single-sided heating wall in terrestrial experiments, particularly in flow boiling studies at different orientations relative to Earth gravity, is to isolate the influence of gravity component perpendicular to the heated wall on two-phase flow structure and heat transfer. It is important to emphasize that the present study is focused mostly on the high heat flux region of nucleate boiling, including CHF, rather than the single-phase liquid and low heat flux nucleate boiling regions.

Fig. 5 shows individual images of flow boiling for single-sided heating along wall H_1 at inlet velocities ranging from $U = 0.1$–1.9 m/s and heat fluxes increasing to CHF. In the upstream region of the heated wall, the incoming liquid is slightly subcooled and requires a short distance to warm up to saturation temperature before beginning to generate small bubbles. The small bubbles are driven along the heated wall by liquid shear and drag forces, and grow in size because of further evaporation as well as coalescence with other bubbles. This upstream activity quickly develops into large vapor patches that mimic a continuous wavy vapor layer along the heated wall. Notice that boiling is sustained mostly in 'wetting fronts' where the wave troughs contact the wall, and abated within the large vapor patches or wave peaks. For each combination of velocity and heat flux, the mean thickness of the wavy vapor layer increases along the flow direction. Comparing images corresponding to different velocities shows the length of vapor patches decreases and number of wetting fronts increases with increasing velocity. These interfacial characteristics are consistent with wavelength trends predicted according to hydrodynamic instability theory as proposed by Galloway and Mudawar [22,23]. Further details concerning CHF mechanism and commencement will be deferred to the second part of this study [19].

Fig. 6 shows 15 sequential images captured for single-sided heating along H_1 for $U = 0.1$, 0.5, 0.9 and 1.9 m/s at the lowest recorded percentage of CHF value as well as close to but below CHF. The time elapsed between consecutive frames is 0.451 ms. Here too, the wavy vapor layer is observed for all flow velocities and heat fluxes from approximately 50% CHF to near CHF commencement. At $U = 0.1$ m/s, low liquid inertia fosters rapid growth of nucleating bubbles near the leading edge of the heated wall with immediate bubble coalescence. The vapor patches are shown propagating downstream along the heated wall, gradually increasing in thickness. The upstream bubble growth decreases with increasing flow velocity, and the onset of nucleation is shifted farther downstream, especially for $U = 1.9$ m/s, where bubble nucleation commences at approximately 20% of the heated length.

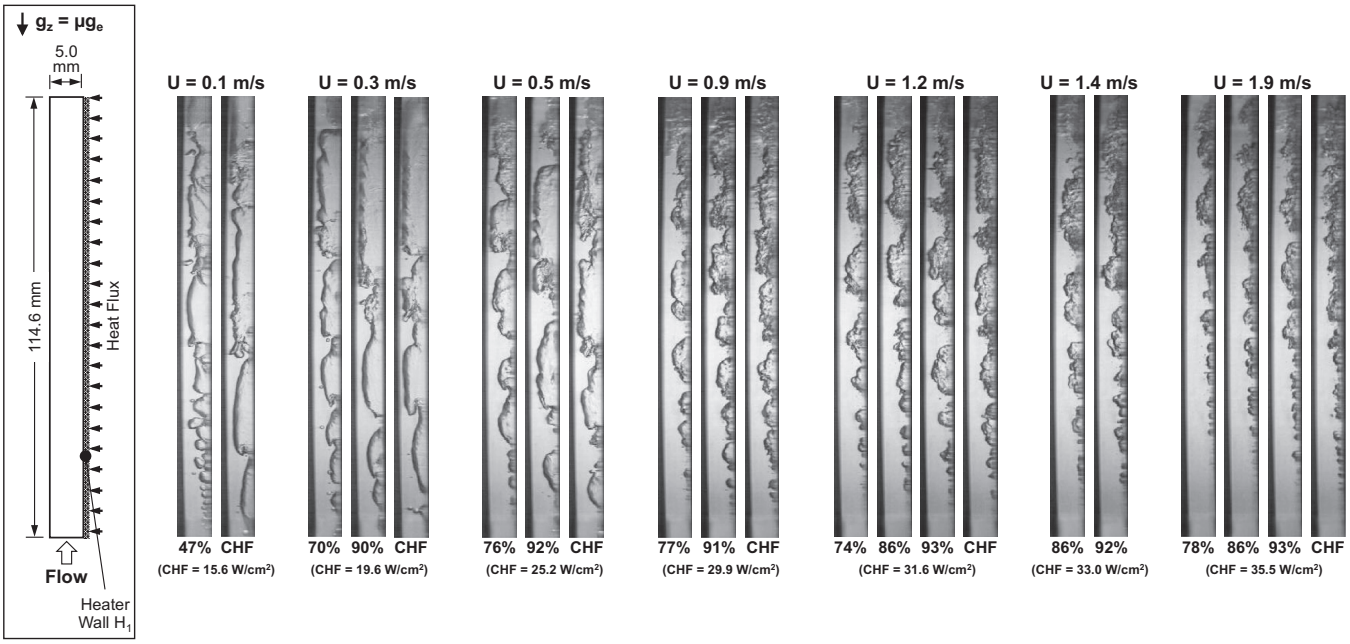

Fig. 5. High-speed video images of heated wall H_1 from single-sided heating experiments for different inlet velocities and different heat fluxes leading to CHF.

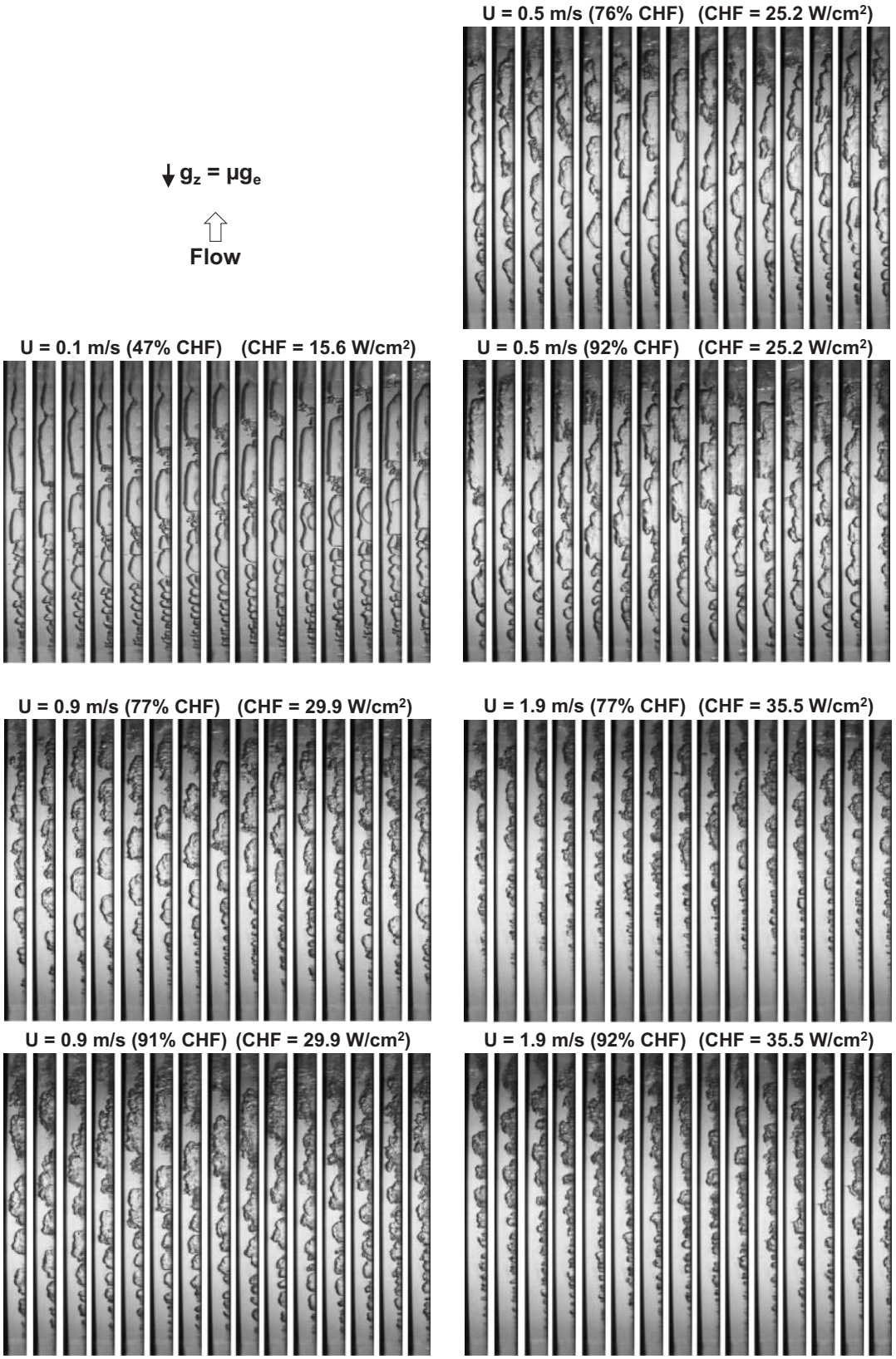

Fig. 6. Sequential high-speed video images of heated wall H_1 from single-sided heating experiments for different inlet velocities and different heat fluxes.

3.2. Interfacial features for double-sided heating

Fig. 7 shows individual images of flow boiling during double-sided heating at inlet velocities ranging from $U = 0.1$–1.9 m/s and heat fluxes increasing to CHF. For each velocity tested, bubble generation culminates in formation of wavy vapor layers on both heated walls. Thickening of the vapor layers along the heated walls causes the two layers to merge downstream. The merger of vapor

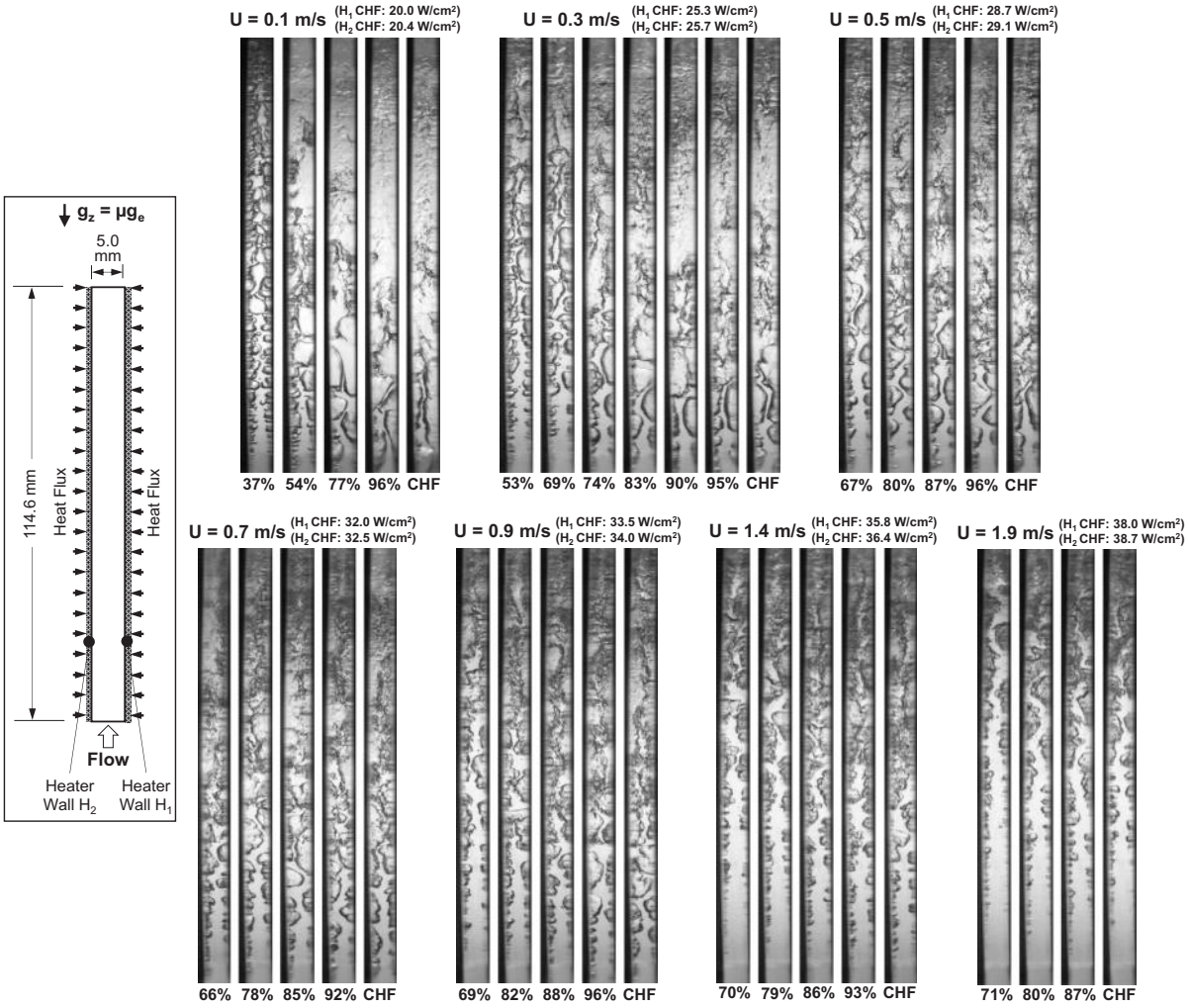

Fig. 7. High-speed video images from double-sided heating experiments for different inlet velocities and different heat fluxes leading to CHF.

layers is observed to shift upstream with increasing heat flux because of the increased vapor production. On the other hand, increasing flow velocity shifts the merger downstream because increased liquid inertia reduces the thicknesses of the individual layers. Notice for the lowest velocity of $U = 0.1$ m/s, a large downstream fraction of the heated length is occupied mostly by vapor, mixed with a few liquid ligaments. For most velocities, CHF occurs as fairly thick vapor layers insulate the downstream regions of the two walls, evidenced by wall temperature excursions in those regions.

Fig. 8 shows 15 sequential high-speed images captured for double-sided heating for $U = 0.1$, 0.5, 0.9 and 1.9 m/s at the lowest recorded percentage of CHF value as well as close to but below CHF. The time elapsed between consecutive frames is 0.451 ms. A low heat flux of 37% CHF is tested only for $U = 0.1$ m/s, where bubbly flow is observed. For all conditions tested, bubble nucleation is initiated very close to the leading edge for both heated walls. The bubbles propagate along the heated walls, gradually growing in size because of both evaporation and coalescence with neighboring bubbles. Eventually, wavy vapor layers are formed on both walls, squeezing the bulk liquid layer in between. The existence of the central liquid layer prevents the two vapor layers from merging fully across the channel. Instead, some vapor bubbles are ejected from one or both heated walls, and are pulled into the bulk liquid layer, possibly by the liquid drag and shear forces. These bubbles are then compressed by the opposite wavy vapor layers and conveyed downstream with the bulk liquid layer. A very interesting behavior is observed as the two opposite wavy vapor layers compete in occupying the channel's cross-section. Upon close examination, the wave peak on one of the heated walls grows rapidly towards the trough (wetting front) between two wave peaks on the opposite wall. Immediately following this event, a wave peak on the second wall immediately upstream grows rapidly towards the trough between two wave peaks on the first heated wall. This phenomenon is constantly repeated, resembling the meshing of mechanical gear teeth between two rotating sprockets. The meshing action between the two opposite wavy vapor layers causes progressive mixing, and culminates in a downstream region occupied mostly by vapor, with remnants of liquid in the form of liquid ligaments. Notice for $U = 0.1$ m/s and 37% CHF, the wavy vapor layers grow at a slow rate, which causes the meshing to take place farther downstream. Increasing the heat input for $U = 0.1$ m/s from 37% to 96% causes the meshing to commence upstream. The same meshing trends are observed for $U = 0.5$, 0.9 and 1.9 m/s. For the highest velocity tested, $U = 1.9$ m/s, high flow inertia significantly delays bubble nucleation and growth of the wavy vapor layers, which causes the meshing to be shifted to the outlet region.

3.3. Idealized depiction of interfacial features for single-sided and double-sided heating

Fig. 9(a) depicts an idealized representation of interfacial behavior for single-sided heating at high heat fluxes approaching

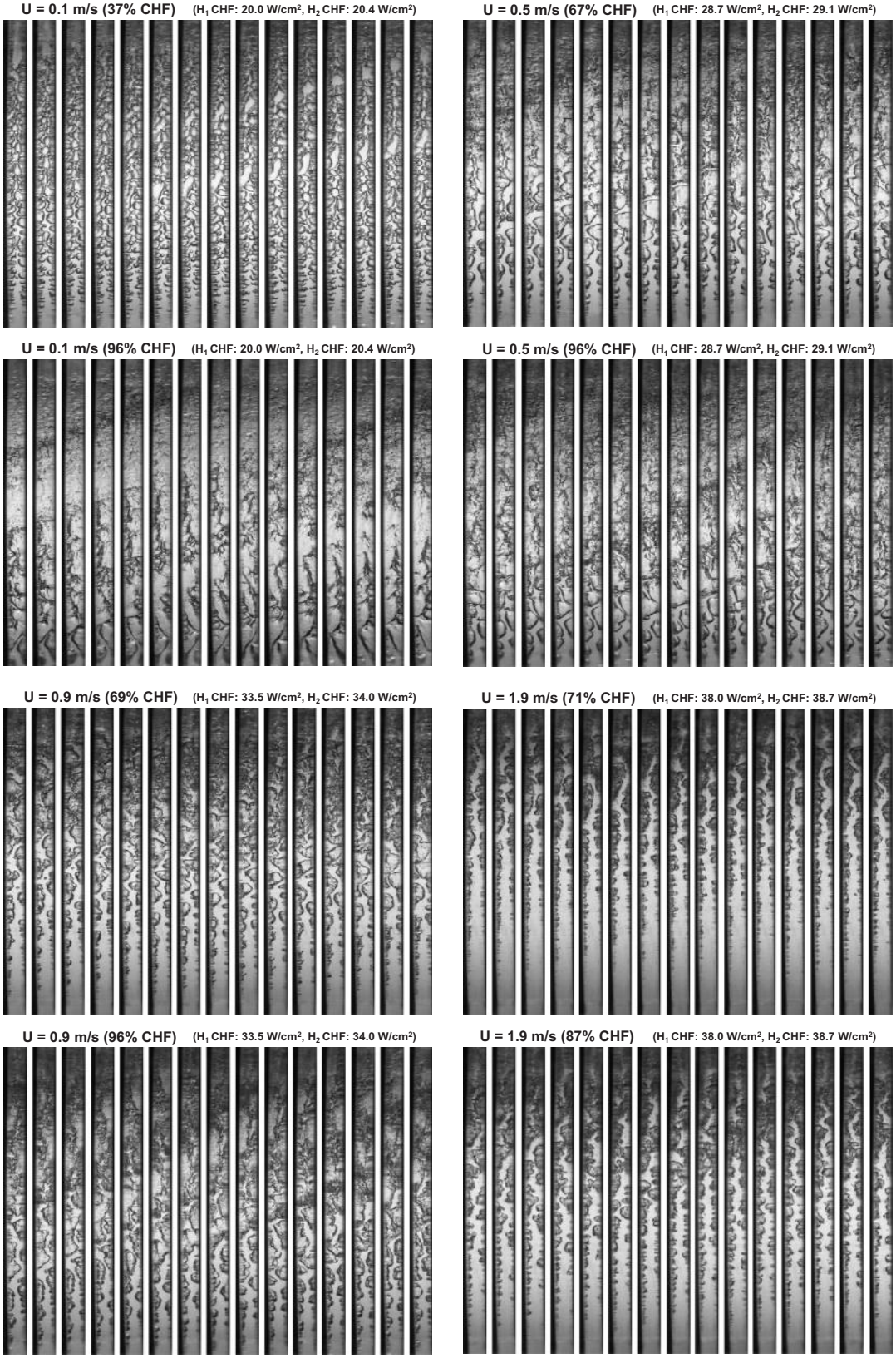

Fig. 8. Sequential high-speed video images from double-sided heating experiments for different inlet velocities and different heat fluxes.

CHF. Near the inlet, subcooled liquid is shown warming up to saturation temperature before bubbles begin to nucleate on heated wall H_1. The bubbles grow quickly due to both evaporation and coalescence with other bubbles, culminating in the formation of a fairly continuous wavy vapor layer. As the vapor layer propagates along the heated wall, dryout occurs beneath the wave peaks, especially close to CHF, while vigorous boiling is sustained in the wave troughs. The mean thickness of the wavy vapor layer

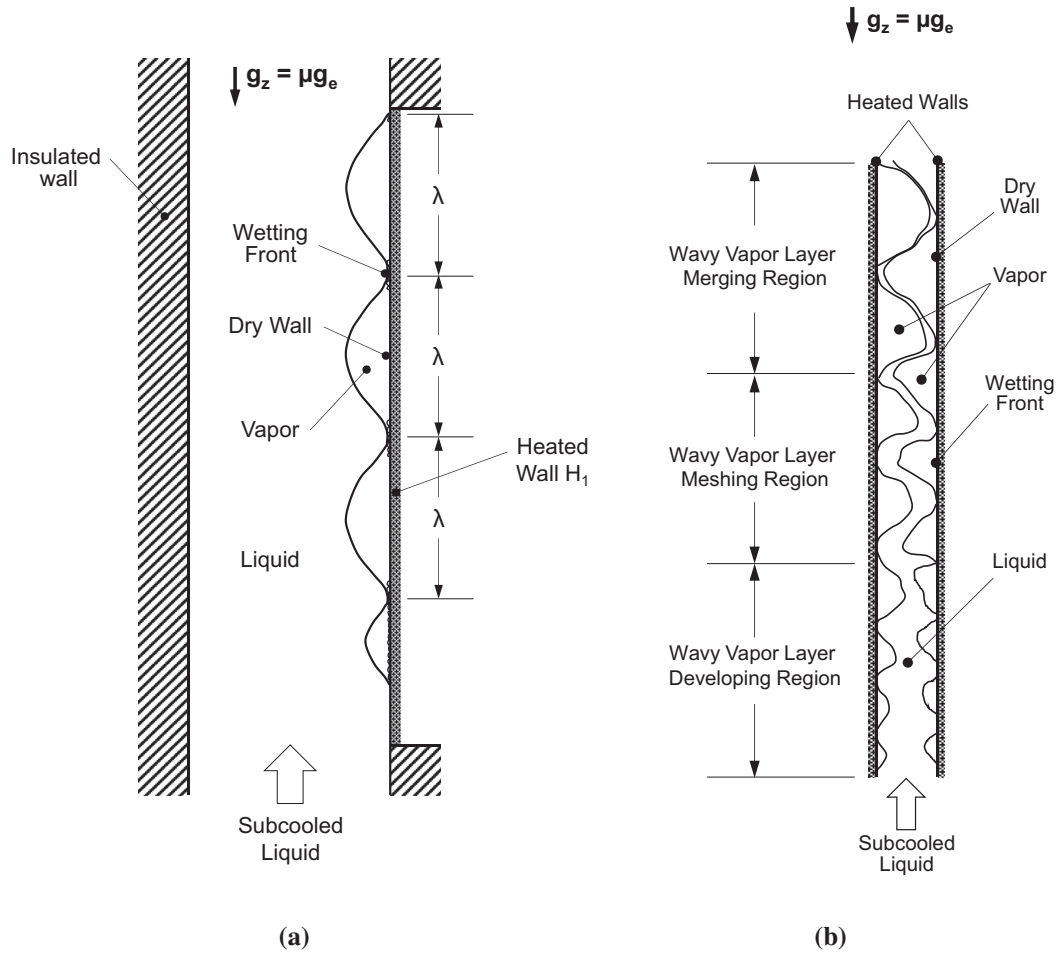

Fig. 9. Schematic representation of pre-CHF interfacial behavior (a) along heated wall H_1 during single-sided heating experiments, and (b) along both walls during double-sided heating experiments.

increases gradually along the heated wall. The axial thickening of the vapor layer is hastened by increasing the heat flux or decreasing the inlet liquid velocity.

Fig. 9(b) depicts an idealized representation of the interfacial behavior captured at high heat fluxes approaching CHF for double-sided heating. Three distinct interfacial flow regions are identified: (1) wavy vapor layer developing region, (2) wavy vapor layer meshing region, and (3) wavy vapor layer merging region. In the upstream wavy vapor layer developing region, subcooled liquid is heated to above saturation temperature, initiating bubble nucleation on both heated walls. The bubbles grow rapidly and coalesce with other bubbles to form a fairly continuous wavy vapor layer. In the middle wavy vapor layer meshing region, wave peaks from one wall protrude towards a trough of the opposite vapor layer. Upon extensive examination of high-speed video records, this phenomenon is observed to occur when the maximum thickness of the wavy vapor layer grows to approximately one-third the distance between the heated walls. Because of the gradual increase in vapor mass flow rate due to evaporation, coupled with the large density differences between the two phases, the vapor layers propagate at a faster rate than the bulk liquid. The combined effect of large interfacial curvature and high velocity difference is speculated to induce flow separation and low pressure zones, which draw in the wave peaks from opposite walls. The downstream wavy vapor layer merging region is characterized by opposite vapor layers virtually merging with one another. Due to low inertia, low flow velocities cause rapid vapor growth, shifting the wavy vapor layer meshing region upstream. Similarly, this region is shifted upstream when the wall heat flux is increased.

4. Heat transfer results

4.1. Experimental heat transfer data reduction

Experimental data are continuously recorded during every parabolic flight. Fig. 10(a)–(c) shows composite temporal plots of heated wall temperatures and heat fluxes, and gravity for double-sided heating at $U = 0.1$ m/s, single-sided heating at $U = 1.9$ m/s, and double-sided heating at $U = 1.9$ m/s, respectively. The temperatures are designated as $T_{w1,n}$ and $T_{w2,n}$, where 1 and 2 refer to heated walls H_1 and H_2, respectively, and n is the thermocouple location along the heated wall. For $U = 0.1$ m/s, Fig. 10(a) shows a slight drop in the heated wall temperatures as the aircraft enters the hypergravity phase of the parabola. The heated wall temperatures then increase slightly as the aircraft enters the microgravity phase, and decrease once again during hypergravity. These temperature variations point to enhancement in flow boiling heat transfer with increasing gravity, and degradation in μg_e. These trends are consistent with those of parabolic flight experiments with FC-72 in a 6.0-mm diameter tube by Baltis et al. [16] corresponding to moderate

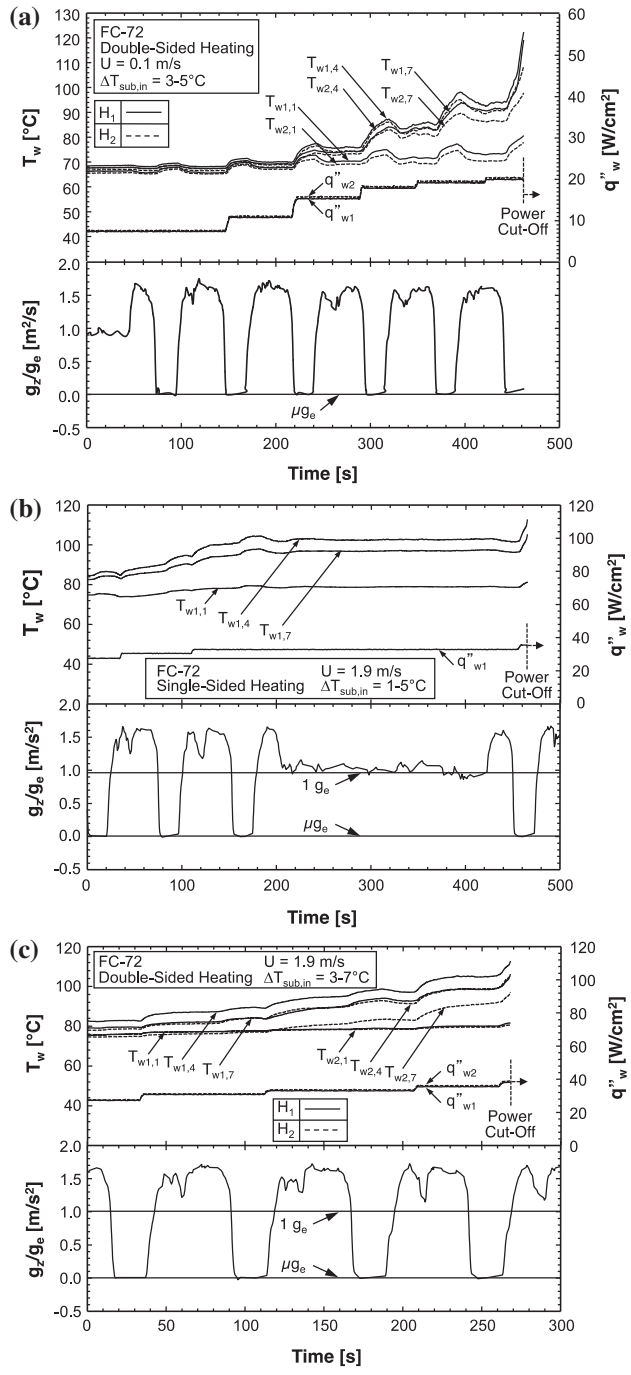

Fig. 10. Temporal records of heated wall temperatures and heat fluxes, and gravity during series of parabolas for (a) double-sided heating at $U = 0.1$ m/s, (b) single-sided heating at $U = 1.9$ m/s, and (c) double-sided heating at $U = 1.9$ m/s.

to high heat fluxes. The temporal plots for $U = 1.9$ m/s in Fig. 10(b) and (c) shows heated wall temperature variations across the hypergravity, while in microgravity and hypergravity descent they are less pronounced than for $U = 0.1$ m/s, Fig. 10(a), because of the reduced influence of gravity at higher velocities. It should be noted that the flow rate changes by approximately 5% while transitioning between different gravitational phases during a parabolic maneuver. This change is attributed to changes in hydrostatic head within the flow loop with varying gravity, and is more pronounced at low velocities and decreases with increasing velocity.

Although data are measured throughout the parabolic maneuver, inconsistencies in the magnitude of hypergravity, coupled with g-jitter due to turbulence and short durations of hypergravity, preclude any reliable measurements during hypergravity. Therefore, all experimental results presented in this study concern the microgravity phase alone. Results are presented both for single-sided and double-sided heating.

4.2. Experimental heat transfer trends

As indicated earlier, the present study is focused mostly on the upper region of the nucleate boiling curve depicted in Fig. 11(a). Data obtained in this region, coupled with high-speed video motion analysis, help provide both qualitative and quantitative identification of mechanisms leading to CHF. Fig. 11(b) and (c) provide, for different inlet velocities, data for the nucleate boiling region preceding CHF for single-sided and double-sided heating, respectively. The wall heat flux, q''_w, is plotted versus the difference between the average wall temperature, $T_{w,avg}$, and saturation temperature, T_{sat}. The single-sided and double-sided data exhibit similar monotonically increasing trends of heat flux with temperature difference, as well as a shift to higher heat fluxes with increasing velocity. Fig. 11(c) shows slight differences in boiling data for heated walls H_1 and H_2, which are attributed to small differences in electrical power input between the arrays of six thick-film resistors soldered to the two walls. These differences are the result of a 0.5-Ω (1.7%) greater equivalent electrical resistance for heated wall H_1 compared to H_2. Comparing Fig. 11(b) and (c) shows better flow boiling performance and as much as 22% higher CHF for double-sided compared to single-sided heating for equal velocities. This heat transfer enhancement with the double-sided heating can be explained as follows. With both walls heated, far more vapor is being produced than with one heated wall. This causes the flow to accelerate much faster, and the heat transfer performance to be enhanced with double-sided versus single-sided heating. Interestingly, Fig. 11(c) shows H_2, which has a slightly higher heat flux, produces lower wall temperatures than H_1. This unexpected trend is speculated to be the result of differences in evaporation rate between the two heated walls. Producing the higher heat flux, H_2 yields higher evaporation rates, increasing flow velocities locally more than along H_1, therefore enhancing heat transfer more and resulting in lower wall temperatures.

Fig. 12(a) and (b) shows, for $U = 0.1$, 0.9 and 1.9 m/s, axial variations of wall temperature for different heat fluxes for single-sided and double-sided heating, respectively. The two heating configurations produce similar trends, with temperatures increasing with increasing heat flux, and, for a fixed heat flux, increasing from the leading edge of the heated wall ($T_{wm,1}$) wall to a maximum immediately downstream from the middle ($T_{wm,5}$ or $T_{wm,6}$), before decreasing again towards the exit ($T_{wm,7}$). As discussed in the second part of this study [19], CHF is initiated in the vicinity of $T_{wm,5}$ or $T_{wm,6}$ where maximum wall temperature is achieved. The lowest wall temperatures at $T_{wm,1}$ are attributed to the fluid entering the heated region as subcooled liquid at the lowest temperature. The wall temperature initially increases downstream of $T_{wm,1}$ as a result of both gradual rise in liquid temperature and vapor layer development. However, the vapor generation also causes gradual acceleration of the flow, which helps enhance heat transfer and therefore decrease wall temperature. The net effect of these two opposing trends is to achieve maximum wall temperature shortly downstream of the middle, before acceleration dominates heat transfer and reduces wall temperature towards the exit. This process is also complicated by the development of the wavy vapor layer along the heated wall for single-sided heating, and both the vapor layer development and meshing between vapor layers for double-sided heating.

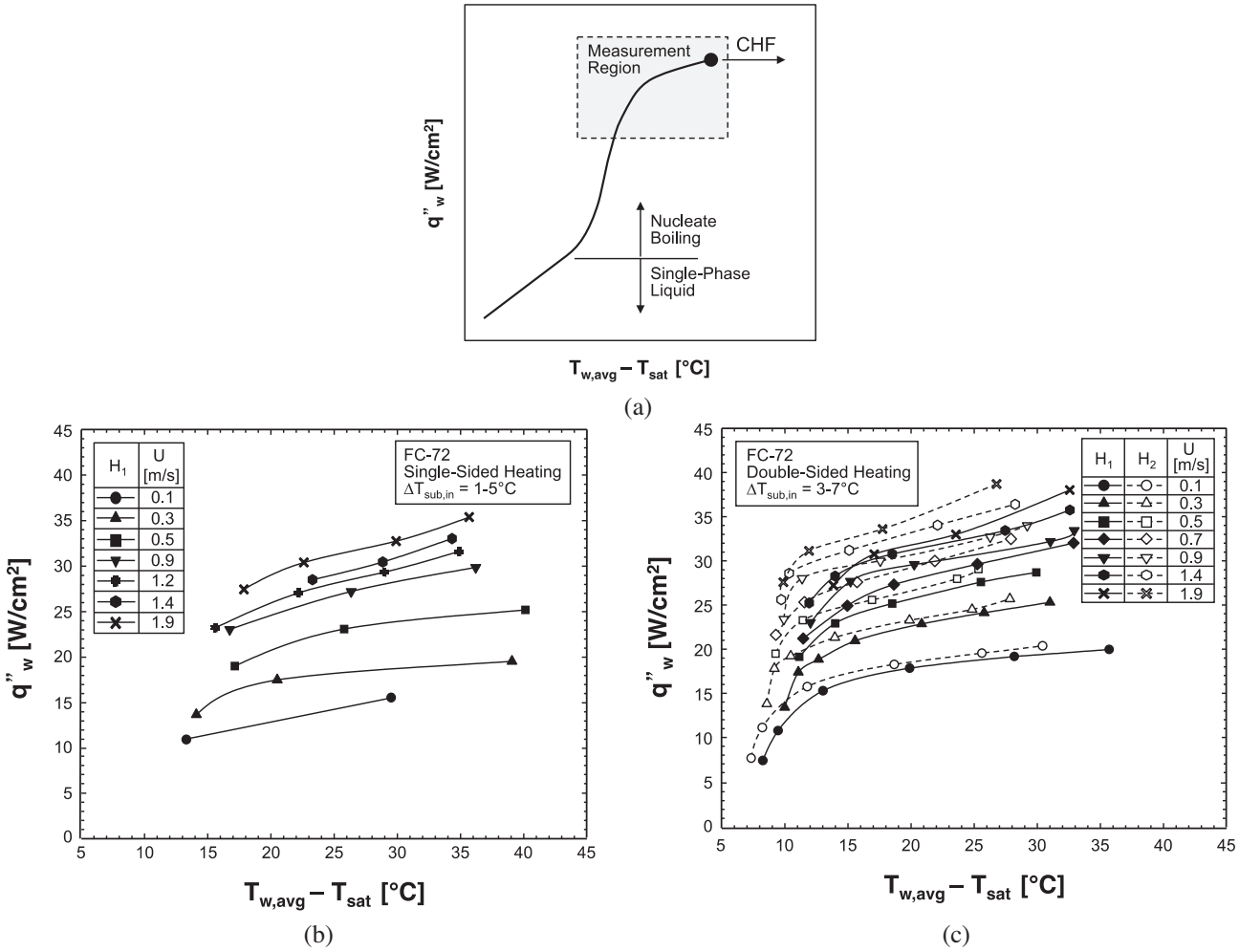

Fig. 11. (a) Region of boiling curve of interest to present study. (b) Boiling curves for heated wall H_1 from single-sided heating experiments for different inlet velocities. (c) Boiling curves for both heated walls from double-sided heating experiments for different inlet velocities.

The local heat transfer coefficient at a wall thermocouple location is obtained from the following expression,

$$h_{m,n} = \frac{q''_w}{(T_{wm,n} - T_f)}, \tag{1}$$

where q''_w is the wall heat flux, $T_{wm,n}$ the wall temperature measured along heated wall m ($m = 1$ for H_1 and 2 for H_2), with n corresponding to thermocouple location z_n, and T_f the bulk fluid temperature. Subcooled liquid enters the heated portion of the channel and is heated up to T_{sat} before bubbles can begin to nucleate. For double-sided heating, axial variations of the bulk fluid temperature, T_f, encompassing the subcooled and saturated regions are given, respectively, by

$$T_{f,n+1} = T_{f,n} + \frac{(q''_{w1} + q''_{w2})\, W \Delta z}{\dot{m} c_{p,f}} \quad \text{for} \quad x_e < 0 \tag{2a}$$

and

$$T_f = T_{sat} \quad \text{for} \quad 0 \leqslant x_e \leqslant 1. \tag{2b}$$

The above equations are also used for single-sided heating by setting $q''_{w2} = 0$. A single value of the heat transfer coefficient is determined at each thermocouple location. These values are then spatially averaged to determine h_{avg}. Table 1 shows calculated values of axial location where $x_e = 0$ for the different operating conditions. The maximum uncertainties in determining the bulk fluid temperature at $x_e = 0$ and h_{avg} are 0.89% and 10.86%, respectively. Figs. 5–8 showed earlier that the axial distances for initiation of the vapor layer are quite small compared to the heated length. The relatively large values for axial location where $x_e = 0$ in Table 1 points to non-equilibrium effects across the flow area of the channel.

Fig. 13(a) and (b) shows variations of h_{avg} with inlet velocity at different heat fluxes for single-sided and double-sided heating, respectively. For single-sided heating, Fig. 13(a) shows h_{avg} increases fairly monotonically with increasing velocity for fixed heat flux, and decreases, for fixed velocity, as heat flux increases towards CHF. For double-sided heating, Fig. 13(b) shows h_{avg} generally increases with increasing inlet velocity for fixed heat flux, and decreases, for fixed velocity, as the heat flux is increased towards CHF. However, there is a slight decline in h_{avg} above 1.4 m/s for 80% and 85% of CHF. Like the boiling curves and temperature data, there are differences in h_{avg} between the two heated walls that generally increase with increasing velocity.

Fig. 14(a) and (b) shows the variations of h_{avg} with heat flux at different inlet velocities for single-sided and double-sided heating, respectively. Overall, h_{avg} increases with increasing velocity. But the variation of h_{avg} with heat flux appears to be governed by evolution of the vapor layer along the heated length. As depicted in the video images, heat transfer from the heated wall to the bulk liquid

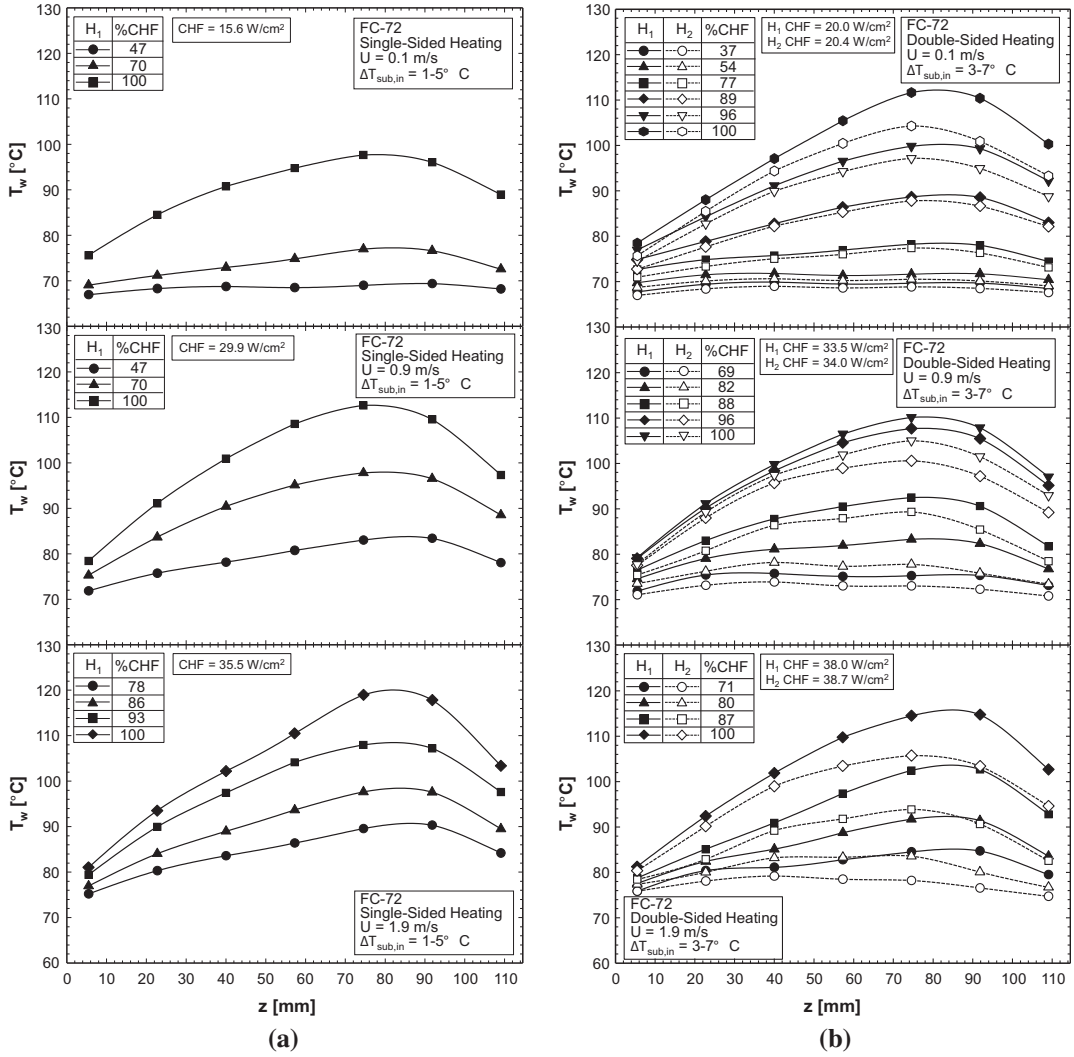

Fig. 12. Variation of temperature along heated wall for different heat fluxes for (a) heated wall H_1 from single-sided heating experiments, and (b) both heated walls from double-sided heating experiments.

Table 1
Axial locations of saturated heated wall regions for both single-sided and double-sided heating experiments.

U (m/s)	$z\|_{x_e=0}$ (mm) (Double-sided heating)	$z\|_{x_e=0}$ (mm) (Single-sided heating)
0.1	7.9–18.3	10.1–15.8
0.3	22.1–44.2	24.3–30.3
0.5	23.2–37.8	64.2–48.3
0.7	31.9–33.5	Pressure not measured
0.9	37.4–64.0	74.8–85.9
1.2	Pressure not measured	68.0–81.7
1.4	51.7–67.3	79.7–90.6
1.9	68.3–85.1	Values exceed heated length

is speculated to occur primarily in the wetting fronts separating less conductive vapor patches. While increasing the heat flux increases flow velocity due to increased evaporation, the wall regions beneath the vapor patches become increasingly dry, placing more pressure on the wetting fronts to dissipate the majority of the heat. This is also exasperated by increased vapor production netting more dryout downstream, which is especially problematic for double-sided heating because of the merging of vapor layers from opposite walls.

These complex trends will be explored in the second part of this study [19] with aid of a separated flow model that will track axial variations of mean velocities and mean thicknesses of the liquid and vapor layers, as well as the theoretical Interfacial Lift-off Model that will assess the impact of these variations on flow boiling CHF.

This study points to the importance of both amassing large databases to better ascertain parametric trends as discussed in [36,37], and better characterizing interfacial behavior. Interfacial waves appear to play a dominant heat transfer role for all conditions tested. Better characterization of these waves will require conducting detailed measurements of liquid velocity and turbulence, and local instantaneous thicknesses of both the liquid and vapor layers. Liquid velocity and turbulence measurements have indeed been conducted in adiabatic, relatively thick wavy liquid films [38,39]. For small channels, liquid velocity measurements are possible with the aid of micro-particle image velocimetry (μ-PIV) [40]. Small channels also require miniaturized sensors to measure liquid and vapor layer thicknesses and characterize interfacial waves [38,39,41], as well as temperature profile across the liquid layer [42–45]. However, it is not known how such complex diagnostic tools might influence flow boiling structure and especially CHF.

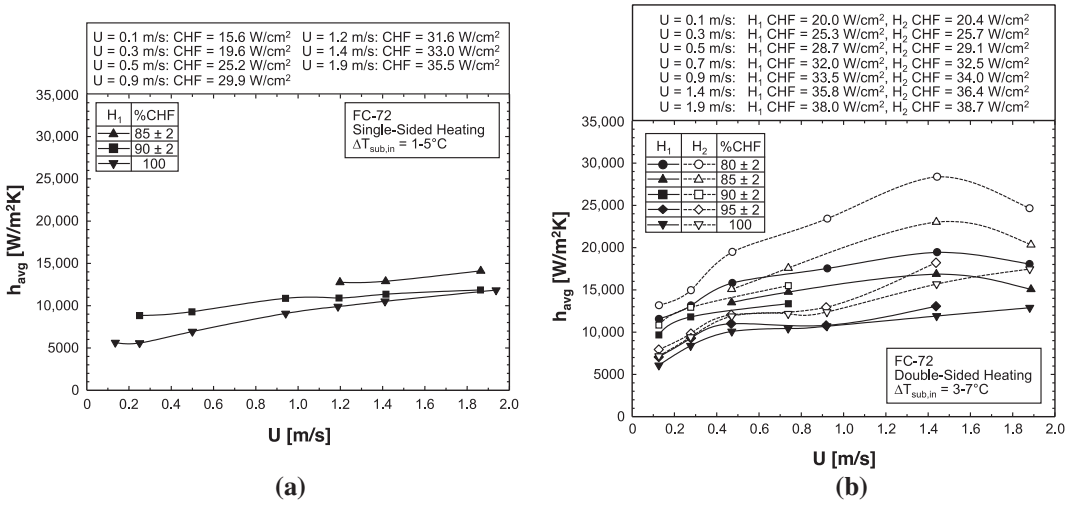

Fig. 13. Variation of heat transfer coefficient with inlet velocity for different heat fluxes for (a) heated wall H_1 from single sided heating experiments, and (b) both heated walls from double-sided heating experiments.

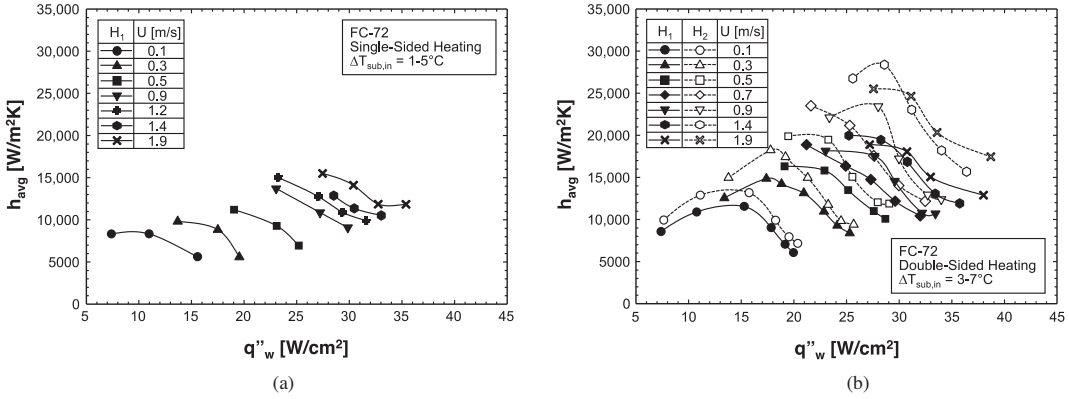

Fig. 14. Variation of heat transfer coefficient with wall heat flux for different inlet velocities for (a) heated wall H_1 from single-sided heating experiments, and (b) both heated walls from double-sided heating experiments.

5. Conclusions

This study explored flow boiling heat transfer of FC-72 in microgravity, which was simulated in a series of parabolic flight maneuvers. A rectangular flow channel was used, which was fitted with two opposite heating walls, allowing either one or both walls to be activated during a given test. The study involved both high-speed video analysis of interfacial features and heat transfer measurements. Key findings from the study are as follows.

(1) Bubbly flow is encountered with double-sided heating only at the lowest flow velocity (U = 0.1 m/s) and lowest heat flux (37% CHF) tested. For all remaining conditions, which include velocities as high as 1.9 m/s and moderate to high heat fluxes, a dominant wavy vapor layer is encountered with both single-sided and double-sided heating. Boiling is sustained mostly in 'wetting fronts' where the wave troughs contact the wall, and abated near the wave peaks. The mean thickness of the vapor layer increases along the heated wall, but the wavelength decreases and number of wetting fronts increases with increasing velocity.

(2) Double-sided heating produces complex interactions between the opposite wavy vapor layers, resulting in three distinct regions: wavy vapor layer developing region, wavy vapor layer meshing region, and wavy vapor layer merging region. The wavy vapor layer is formed initially in the upstream developing region. In the middle meshing region, wave peaks from one wall protrude towards troughs in the opposite vapor layer, mimicking the engagement of gear teeth. The downstream merging region is characterized by opposite vapor layers virtually merging with one another with liquid ligaments squeezed in between.

(3) During a flight parabola, heated wall temperatures decrease slightly as the aircraft enters the hypergravity phase of the parabola. The heated wall temperatures then increase slightly as the aircraft enters the microgravity phase, and decrease once again during the hypergravity. These temperature variations point to enhancement in flow boiling heat transfer with increasing gravity, and degradation in μg_e.

(4) For identical inlet velocities and equal heat fluxes, double-sided heating produces better heat transfer compared to single-sided. This enhancement is attributed to higher vapor production, with double-sided heating resulting in faster fluid motion.

Conflict of interest

None declared.

Acknowledgment

The authors are grateful for the support of this project by the National Aeronautics and Space Administration (NASA) – United States under Grant no. NNX13AB01G.

References

[1] F.P. Chiaramonte, J.A. Joshi, Workshop on critical issues in microgravity fluids, transport, and reaction processes in advanced human support technology – final report, NASA TM-2004-212940, 2004.
[2] The National Academies, Recapturing a future for space exploration: life and physical sciences research for a new era, National Academies Press, Washington, DC, 2011.
[3] T. Oka, Y. Abe, Y.H. Mori, A. Nagashima, Pool boiling of n-Pentane, CFC-113, and water under reduced gravity: parabolic flight experiments with a transparent heater, J. Heat Transfer – Trans. ASME 117 (1995) 408–417.
[4] J. Straub, G. Picker, M. Steinbichler, Boiling and bubble dynamics at a small hemispherical heater under microgravity and Earth conditions, in: University of Tokyo, Second Japanese-German Symp. Multi-Phase-Flow, Tokyo, Japan, 1997, pp. 169–176.
[5] H. Merte, Momentum effects in steady nucleate pool boiling during microgravity, Ann. N.Y. Acad. Sci. 1027 (2004) 196–216.
[6] J. Kim, J.F. Benton, D. Wisniewski, Pool boiling heat transfer on small heaters: effect of gravity and subcooling, Int. J. Heat Mass Transfer 45 (2002) 3919–3932.
[7] V.K. Dhir, G.R. Warrier, E. Aktinol, D.F. Chao, J. Eggers, W. Sheredy, W. Booth, Nucleate pool boiling experiments (NPBX) on the International Space Station, Microgravity Sci. Technol. 24 (2012) 307–325.
[8] D.B. Hepner, C.D. King, J.W. Littles, Zero gravity experiments in two-phase fluids flow regimes, in: ASME Intersociety Conf. Environmental Systems, San Francisco, CA, 1975.
[9] A.E. Dukler, J.A. Fabre, J.B. McQuillen, R. Vernon, Gas–liquid flow at microgravity conditions: flow patterns and their transitions, Int. J. Multiphase Flow 14 (1988) 389–400.
[10] C. Colin, J. Fabre, A.E. Dukler, Gas–liquid flow at microgravity conditions – I. Dispersed bubble and slug flow, Int. J. Multiphase Flow 17 (1991) 533–544.
[11] M. Misawa, An experimental and analytical investigation of flow boiling heat transfer under microgravity conditions (Ph.D. thesis), University of Florida, 1993.
[12] M. Saito, N. Yamaoka, K. Miyazaki, M. Kinoshita, Y. Abe, Boiling two-phase flow under microgravity, Nucl. Eng. Des. 146 (1994) 451–461.
[13] H. Ohta, Experiments on microgravity boiling heat transfer by using transparent heaters, Nucl. Eng. Des. 175 (1997) 167–180.
[14] G.P. Celata, M. Cumo, M. Gervasi, G. Zummo, Flow pattern analysis of flow boiling in microgravity, Multiphase Sci. Technol. 19 (2007) 183–210.
[15] G.P. Celeta, M. Cumo, M. Gervasi, G. Zummo, Quenching experiments inside 6.0 mm tube at reduced gravity, Int. J. Heat Mass Transfer 52 (2009) 2807–2814.
[16] C. Baltis, G.P. Celeta, M. Cumo, L. Saraceno, G. Zummo, Gravity influence on heat transfer rate in flow boiling, Multiphase Sci. Technol. 24 (2012) 203–213.
[17] S. Luciani, D. Brutin, C. Le Niliot, O. Rahli, L. Tadrist, Flow boiling in minichannels under normal, hyper-, and microgravity: local heat transfer analysis using inverse methods, J. Heat Transfer – Trans. ASME 130 (2008) 1–13.
[18] S. Luciani, D. Brutin, C. Le Niliot, O. Rahli, Boiling heat transfer in a vertical microchannel: local estimation during flow boiling with a non intrusive method, Multiphase Sci. Technol. 21 (2009) 297–328.
[19] C. Konishi, H. Lee, I. Mudawar, M.M. Hasan, H.K. Nahra, N.R. Hall, J.D. Wagner, R.L. May, J.R. Mackey, Flow boiling in microgravity: Part 2 – Critical heat flux interfacial behavior, experimental data, and model, Int. J. Heat Mass Transfer 81 (2015) 721–736.
[20] H. Zhang, I. Mudawar, M.M. Hasan, Flow boiling CHF in microgravity, Int. J. Heat Mass Transfer 48 (2005) 3107–3118.
[21] I. Mudawar, A.H. Howard, C.O. Gersey, An analytical model for near-saturated pool boiling CHF on vertical surfaces, Int. J. Heat Mass Transfer 40 (1997) 2327–2339.
[22] J.E. Galloway, I. Mudawar, CHF mechanism in flow boiling from a short heated wall. Part 1 – Examination of near-wall conditions with the aid of photomicrography and high-speed video imaging, Int. J. Heat Mass Transfer 36 (1993) 2511–2526.
[23] J.E. Galloway, I. Mudawar, CHF mechanism in flow boiling from a short heated wall. Part 2 – Theoretical CHF model, Int. J. Heat Mass Transfer 36 (1993) 2527–2540.
[24] J.C. Sturgis, I. Mudawar, Critical heat flux in a long, rectangular channel subjected to onesided heating. I: Flow visualization, Int. J. Heat Mass Transfer 42 (1999) 1835–1847.
[25] J.C. Sturgis, I. Mudawar, Critical heat flux in a long, rectangular channel subjected to onesided heating. II: Analysis of critical heat flux data, Int. J. Heat Mass Transfer 42 (1999) 1849–1862.
[26] C.O. Gersey, I. Mudawar, Effects of heater length and orientation on the trigger mechanism for near-saturated flow boiling CHF. I: Photographic and statistical characterization of the near-wall interfacial features, Int. J. Heat Mass Transfer 38 (1995) 629–642.
[27] C.O. Gersey, I. Mudawar, Effects of heater length and orientation on the trigger mechanism for near-saturated flow boiling CHF. II: CHF model, Int. J. Heat Mass Transfer 38 (1985) 643–654.
[28] H. Zhang, I. Mudawar, M.M. Hasan, Experimental assessment of the effects of body force, surface tension force, and inertia on flow boiling CHF, Int. J. Heat Mass Transfer 45 (2002) 4079–4095.
[29] H. Zhang, I. Mudawar, M.M. Hasan, Experimental and theoretical study of orientation effects on flow boiling CHF, Int. J. Heat Mass Transfer 45 (2002) 4463–4478.
[30] H. Zhang, I. Mudawar, M.M. Hasan, Investigation of interfacial behavior during the flow boiling CHF transient, Int. J. Heat Mass Transfer 47 (2004) 1275–1288.
[31] H. Zhang, I. Mudawar, M.M. Hasan, Photographic study of high-flux subcooled flow boiling and critical heat flux, Int. Commun. Heat Mass Transfer 34 (2007) 653–660.
[32] C. Konishi, I. Mudawar, M.M. Hasan, Investigation of the influence of orientation on critical heat flux for flow boiling with two-phase inlet, Int. J. Heat Mass Transfer 61 (2013) 176–190.
[33] H. Zhang, I. Mudawar, M.M. Hasan, CHF model for subcooled flow boiling in Earth gravity and microgravity, Int. J. Heat Mass Transfer 50 (2007) 4039–4051.
[34] H. Zhang, I. Mudawar, M.M. Hasan, Assessment of dimensionless CHF correlations for subcooled flow boiling in microgravity and reduced gravity, Int. J. Heat Mass Transfer 50 (2007) 4568–4580.
[35] H. Zhang, I. Mudawar, M.M. Hasan, Application of flow boiling for thermal management of electronics in microgravity and reduced gravity systems, IEEE Trans. – CPMT: Compon. Packag. Technol. 32 (2009) 466–477.
[36] D.D. Hall, I. Mudawar, Ultra-high critical heat flux (CHF) for subcooled water flow boiling. II: High-CHF database and design parameters, Int. J. Heat Mass Transfer 42 (1999) 1429–1456.
[37] D.D. Hall, I. Mudawar, Critical heat flux (CHF) for water flow in tubes. I: Compilation and assessment of world CHF data, Int. J. Heat Mass Transfer 43 (2000) 2573–2604.
[38] I. Mudawar, R.A. Houpt, Mass and momentum transport in smooth falling liquid films laminarized at relatively high Reynolds numbers, Int. J. Heat Mass Transfer 36 (1993) 3437–3448.
[39] I. Mudawar, R.A. Houpt, Measurement of mass and momentum transport in wavy-laminar falling liquid films, Int. J. Heat Mass Transfer 36 (1993) 4151–4162.
[40] W. Qu, I. Mudawar, S.-Y. Lee, S.T. Wereley, Experimental and computational investigation of flow development and pressure drop in a rectangular micro-channel, J. Electron. Packag. – Trans. ASME 128 (2006) 1–9.
[41] J.E. Koskie, I. Mudawar, W.G. Tiederman, Parallel-wire probes for measurement of thick liquid films, Int. J. Multiphase Flow 15 (1989) 521–530.
[42] J.A. Shmerler, I. Mudawar, Local heat transfer coefficient in wavy free-falling turbulent liquid films undergoing uniform sensible heating, Int. J. Heat Mass Transfer 31 (1988) 67–77.
[43] J.A. Shmerler, I. Mudawar, Local evaporative heat transfer coefficient in turbulent free-falling liquid films, Int. J. Heat Mass Transfer 31 (1988) 731–742.
[44] T.H. Lyu, I. Mudawar, Statistical investigation of the relationship between interfacial waviness and sensible heat transfer to a falling liquid film, Int. J. Heat Mass Transfer 34 (1991) 1451–1464.
[45] T.H. Lyu, I. Mudawar, Determination of wave-induced fluctuations of wall temperature and convective heat transfer coefficient in the heating of a turbulent falling liquid film, Int. J. Heat Mass Transfer 34 (1991) 2521–2534.